Selective electrochemical synthesis of urea from nitrate and CO₂ via relay catalysis on hybrid catalysts

Yuting Luo[1,4], Ke Xie[1,4], Pengfei Ou[1,4], Tao Peng[1], Zhu Chen[1], Zhiyuan Zhang[2], Xiao-Yan Li[1], Ivan Grigioni[1], Bilu Liu[2], Dave Sinton[3], Edward H. Sargent[1,†]

1 Department of Electrical and Computer Engineering, University of Toronto, 35 St. George St., Toronto, Ontario M5S 1A4, Canada.

2 Shenzhen Geim Graphene Center, Tsinghua-Berkeley Shenzhen Institute & Institute of Materials Research, Shenzhen International Graduate School, Tsinghua University, Shenzhen 518055, P. R. China.

3 Department of Mechanical and Industrial Engineering, University of Toronto, 5 King's College Rd., Toronto, Ontario M5S 3G8, Canada.

4 These authors contributed equally to this work.

†Corresponding author. Email: ted.sargent@utoronto.ca (E.H.S.)

Abstract

The nitrogen cycle needed for scaled agriculture relies on energy- and carbon-intensive processes and generates nitrate-containing wastewater. Electrochemical co-electrolysis of nitrate widely found in industrial wastewater and agricultural runoff; along with CO_2; enables electrified synthesis of urea and is accompanied by wastewater denitrification. This reaction is multistep, involving 16 electron transfer, and suffers from low selectivity, especially at realistic nitrate concentrations. Here we report a strategy to increase the selectivity to urea using a hybrid catalyst, in which two classes of sites stabilize independently the key intermediates needed in urea formation, $*CO_2NO_2$ and $*COOHNH_2$. When we implement and optimize the Zn/Cu hybrid catalyst, we achieve a record in faradaic efficiencies to of 75% at wastewater level nitrate concentrations (1000 ppm NO_3^- [N]) – this compared to <20% faradaic efficiency in the most efficient prior related reports. Experiments and density functional theory calculations reveal a relay catalysis mechanism wherein $*CO_2NO_2$, the key intermediate for C–N coupling, preferentially forms on Zn sites, and the ensuing protonation step to form $*COOHNH_2$ benefits from a lowered reaction energy on nearby Cu sites.
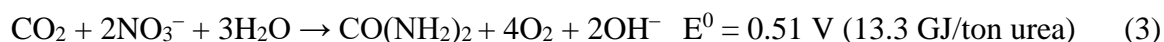
In 2020, anthropogenically activated nitrogen reached ~150 million tons (Mt), 2.5 times the production above the natural baseline[1] (60 Mt). Anthropogenic nitrogen activation starts by converting dinitrogen (N_2) and steam-methane-reformed hydrogen (H_2) to ammonia via the Haber-Bosch process at elevated temperatures (>350 °C) and at very high pressures (>10 MPa).[2] Ammonia is then further processed to nitrogen-containing chemicals (Fig. 1a)[3-5] including urea (for which fully 60% of ammonia production is employed), with urea having an annual production of about 114 Mt. This accounts for 1% of global annual energy consumption and emits net CO_2 of over 270 Mt each year.

Nitrogen-containing waste generated by human activities must be deactivated to N_2 via biological[6] (wastewater) or thermocatalytic[7] (waste gas) processes before it is discharged, and this contributes a further 2% of energy consumption of and 0.5% of global greenhouse gas emissions[6]. The nitrogen activation/deactivation cycle (Fig. 1b) is energy-intensive as a result of the reliance on an inert mediator (N $\equiv$ N bond, 941 KJ mol^{-1}).

The electrochemical conversion of activated-nitrogen-containing wastes (nitrate, nitrile, NO_x,) offers an alternative nitrogen cycle, one that can potentially be implemented under mild conditions (Fig. 1c): nitrate to urea achieved by co-feeding CO_2[5, 8-14]. Nitrate (NO_3^-) from industrial wastewater and agricultural runoff[15, 16] can be converted to urea via a two-step approach:

$$NO_3^- + 2H_2O \rightarrow NH_3 + 2O_2 + OH^- \quad E^0 = 0.53 \text{ V (13.7 GJ/ton urea)} \quad (1)$$

$$2NH_3 + CO_2 \rightarrow CO(NH_2)_2 + H_2O \quad \text{Bosch-Meiser process (practical): 7.1 GJ/ton urea} \quad (2)$$

or a one-step approach:

$$CO_2 + 2NO_3^- + 3H_2O \rightarrow CO(NH_2)_2 + 4O_2 + 2OH^- \quad E^0 = 0.51 \text{ V (13.3 GJ/ton urea)} \quad (3)$$

As shown in Figure 1d, the one-step electrosynthesis of urea from NO_3^- and CO_2 could be interesting if it can be achieved at modest overpotentials, offering an advantage in overall energetics compared to the two-step and the industrial approaches[17, 18] (Supplementary Note 1 and Tables 1-2).
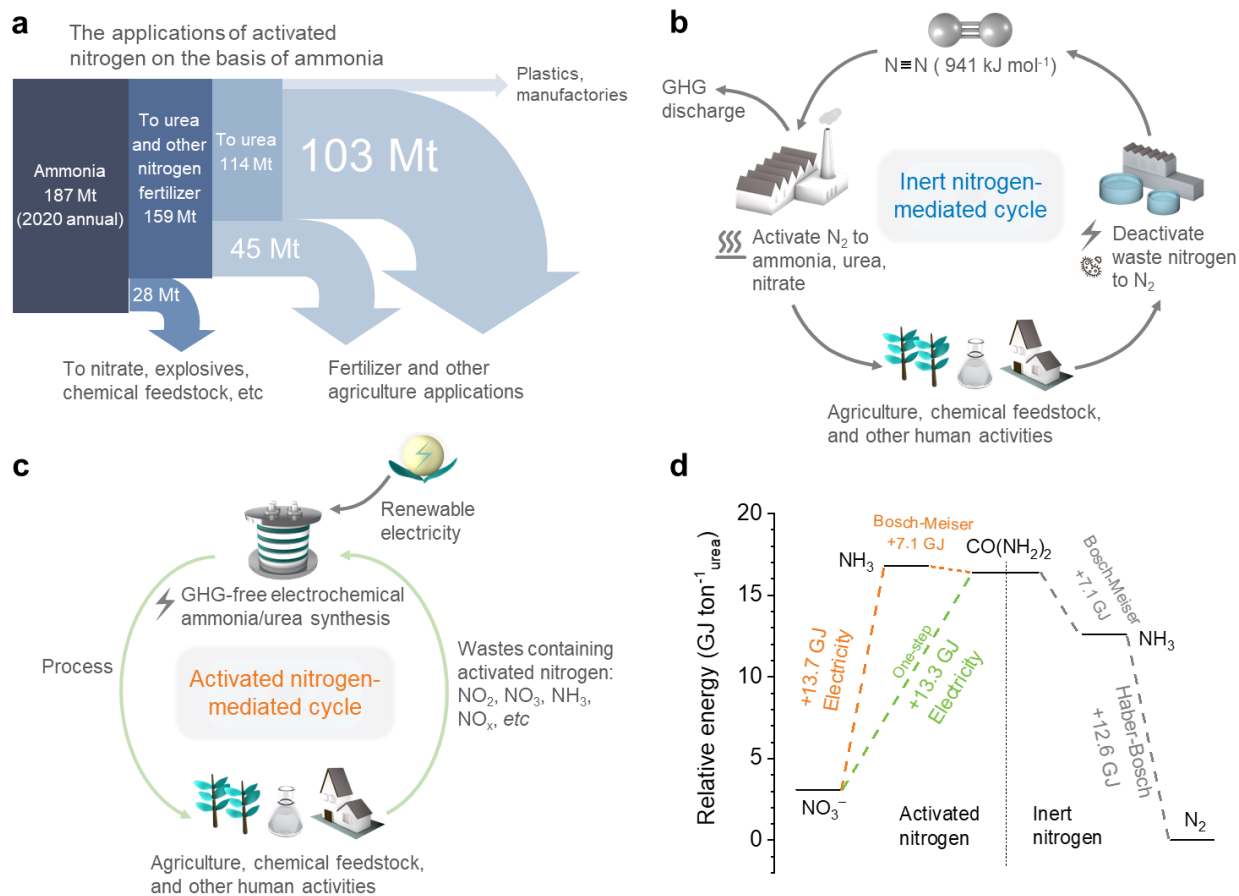
Fig. 1| Nitrogen cycles and their energetics. a) Present-day ammonia and urea volumes and uses[1,2]. **b)** The existing inert-nitrogen (N_2) mediated cycle. **c)** The proposed activated-nitrogen cycle based on nitrate, NO_3^-. **d)** Energy requirements for one-step (green) and two-step (orange) urea electrosynthesis processes and energy requirements for industrial production of urea (grey).

Achieving this shift to a new and potentially more efficient nitrogen cycle will require the development of electrocatalysts exhibiting high urea selectivity via the co-electrolysis of NO_3^- and CO_2. The catalysts should provide C–N coupling while minimizing side reactions from nitrate (NO_3RR), CO_2 (CO_2RR), and H_2O (HER). Previous studies have reported catalysts capable of producing urea from NO_3^- and CO_2,[5, 10, 19, 20] but these have been limited to < 20% faradaic efficiency when realistic nitrate concentrations are employed (such as 200 ppm), for HER becomes dominant (Supplementary Table 3). Simultaneous adsorption of NO_3^- and CO_2 onto the catalyst is needed for C–N coupling, but then the competing single-precursor reductions, NO_3RR to N_2 or

NH$_3$[21], and CO$_2$RR to CO[20], then take over, militating against the desired high selectivity to a single desired product, urea.

Synthesizing urea from NO$_3^-$ by co-feeding CO$_2$ is a multistep reaction involving 16 electrons to be transferred for each urea molecule. The first C–N bond formation (intermediate *CO$_2$NO$_2$) and the protonation of *CO$_2$NH$_2$ (intermediate *COOHNH$_2$) are two key steps of urea formation[5]. The relative reaction energies of the steps are correlated as described via scaling relations, suggesting the need instead for independent tailoring of the reaction energy for distinct sites, and a handoff of key intermediates among sites, in order to circumvent the scaling relations.

We first screened single-component metals known to prefer CO$_2$RR and NO$_3$RR over HER. We found that Cu, Sn, Bi, Zn, and Ag enable modest levels of urea synthesis, with Faradaic efficiencies to urea (FEs) < 20% at 500 ppm NO$_3^-$ [N] (Fig. 2c). To diagnose their low selectivity to urea, we then employed density functional theory (DFT) calculations to analyze reaction pathway for the co-electrolysis of NO$_3^-$ and CO$_2$ on some of the single-component metals (Supplementary Fig. 1). The adsorption of *NO$_2$ is energetically favored on these metal surfaces, followed by either a first C–N bond formation step (*CO$_2$NO$_2$) or the reduction of *NO$_2$[5]. The reaction energy for such a C–N bond formation step is much smaller on Zn surface than on that the Cu or Ag. The reaction energy for the protonation step (*COOHNH$_2$), however, is smaller on Cu or Ag surfaces than it is on Zn. This explains low urea FEs on single-component metals and offers an account of the higher performance of multi-component catalysts.

This motivated us to explore hybrid catalysts, where the first class of sites would lower the barrier energy for the C–N bond formation step, and a second would reduce that for the protonation step to produce urea (Fig. 2a). We then screened hybrid catalysts composed of pairs of the same list of metals (Fig. 2c). Among them, Zn/Cu (64%) and Zn/Ag (44%) showed striking improvements compared to single-component catalysts.

We then sought to transfer the Zn/Cu hybrid catalyst to a gas diffusion layer (GDL) architecture, with a portion of Cu (Fig. 2b and Supplementary Figs. 2-3) readily accessible to reactants and intermediates in the liquid phase, the exposed Cu achieved by spray-coating an incomplete layer of Zn atop the Cu layer. As seen in X-ray diffraction (XRD) and high-resolution transmission electron microscopy (HR-TEM), Zn/Cu hybrid catalysts are based on metallic phases

with predominant crystalline facets Cu (111), Cu (200), Zn (002), and Zn (101) (Supplementary Figs. 4-5).
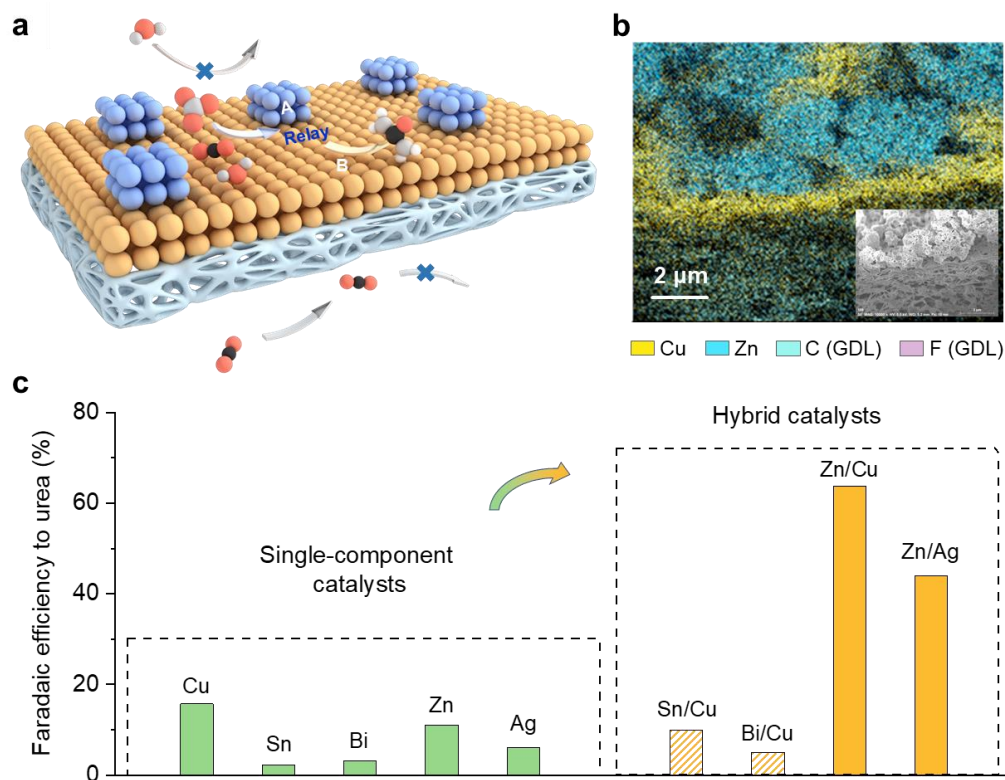

Fig. 2| Screening of single-component and hybrid catalysts. a) Hybrid catalyst wherein one component lowers the reaction energy of the C–N bond formation step, and a second component reduces the reaction energy of the protonation step needed to produce urea. Red, dark, grey and white denote O, C, N and H. **b)** EDS mapping of a Zn/Cu hybrid catalyst. **c)** Screening of single-component catalysts and hybrid catalysts.

We evaluated urea electrosynthesis performance in the electrolytes containing KNO_3 (500 ppm N) and $KHCO_3$ (0.1 M), saturated by CO_2. We fed CO_2 into the electrochemical system from a GDL (Supplementary Fig. 6). To quantify urea production, we used UV-vis absorption spectrophotometry, [14]N Nuclear Magnetic Resonance (NMR), and isotope ^{15}N NMR (Fig. 3a, Supplementary Figs. 7-9). The best hybrid catalysts exhibit urea FEs of $64 \pm 3\%$ (Fig. 3a), higher than that of single-component Cu and Zn (FEs <15%, Fig. 2a). Controls (Supplementary Fig. 10) indicate the need for electrons (e[−]), NO_3^- in the electrolyte, and gaseous CO_2.

We then investigated C–N coupling preference on Zn, Cu and Zn/Cu hybrid catalysts by comparing their urea FEs relative to other reactions. The ratios between $FE_{C–N-coupling}$ and $FE_{non-C–N-coupling}$ indicate selectivity to C–N coupling compared to non-C–N-coupling reactions (Fig. 2b). HER and CO_2RR predominate on single-component Zn and Cu catalysts. CO_2 is mainly converted to formate on the Zn catalyst and C_{2+} products on Cu (Supplementary Fig. 11). In contrast, the Zn/Cu hybrid catalyst exhibits $FE_{CO2RR}/FE_{C–N-coupling}$ and $FE_{HER}/FE_{C–N-coupling}$ of 0.13 and 0.16. Considerable NO_3RR-produced ammonia was detected only on Cu.

We optimized the Zn and Cu components. X-ray photoelectron spectroscopy (XPS) shows atomic ratios of Zn:Cu on the surfaces are from about 0.4 (0.2 mg cm^{-2} Zn) to 1.4 (0.5 mg cm^{-2} Zn) and 7.8 (2.2 mg cm^{-2} Zn) as loading of Zn increases (Supplementary Fig. 12). Only NO_3RR products are detected when we employ a pure-Cu catalyst. When we loaded with even a small amount of Zn (above 0.1 mg cm^{-2}), the Zn/Cu hybrid catalyst shows undetectable NO_3RR products (NH_3, N_2, N_2O, NO, etc, Supplementary Fig. 13). When we increased Zn loading above 0.8 mg cm^{-2}, we saw much formate, acetic acid, and hydrogen (FEs of 5%, 16%, and 28%, Supplementary Fig. 14). Formate and hydrogen become the major products (FEs of 18% and 25%) when Zn loading increases to 1 mg cm^{-2}. We did not detect CO on any hybrid catalyst.

The selectivity to urea on Zn/Cu hybrid catalysts was also optimized with the aid of systematic variations in electrode configuration (Supplementary Fig. 16). Reversing the positions of Zn and Cu on carbon paper (Cu on the top of Zn, Cu/Zn) led to decreased urea FE from 42% to 24%, with increased H_2 accounting for the difference.

We then further studied catalytic performance of the optimized catalyst, Zn-0.5/Cu. The product distribution is potential-dependent (Fig. 3c), peaking at –0.6 V vs. RHE, a finding we assign to faster HER kinetics at higher overpotentials (Supplementary Fig. 18). The competition of HER predominates when the potential is below -0.8 V vs. RHE (Supplementary Fig. 17). The urea FEs of Zn/Cu hybrid catalysts are higher than those of the best previously-reported electrocatalysts to urea (Supplementary Table 3).

We studied catalytic performance of Zn-0.5/Cu at different realistic concentrations of nitrate (Fig. 3d). HER diminishes as the nitrate concentration increases and CO_2RR does not change much. The urea selectivity varies from 50% at 100 ppm N to 75% at 1000 ppm N.

We evaluated stability under –0.6 V vs. RHE at 500 ppm [N]. The current density does not change to within 5% relative, and the urea FE was maintained to within 4% absolute after 8 hours.
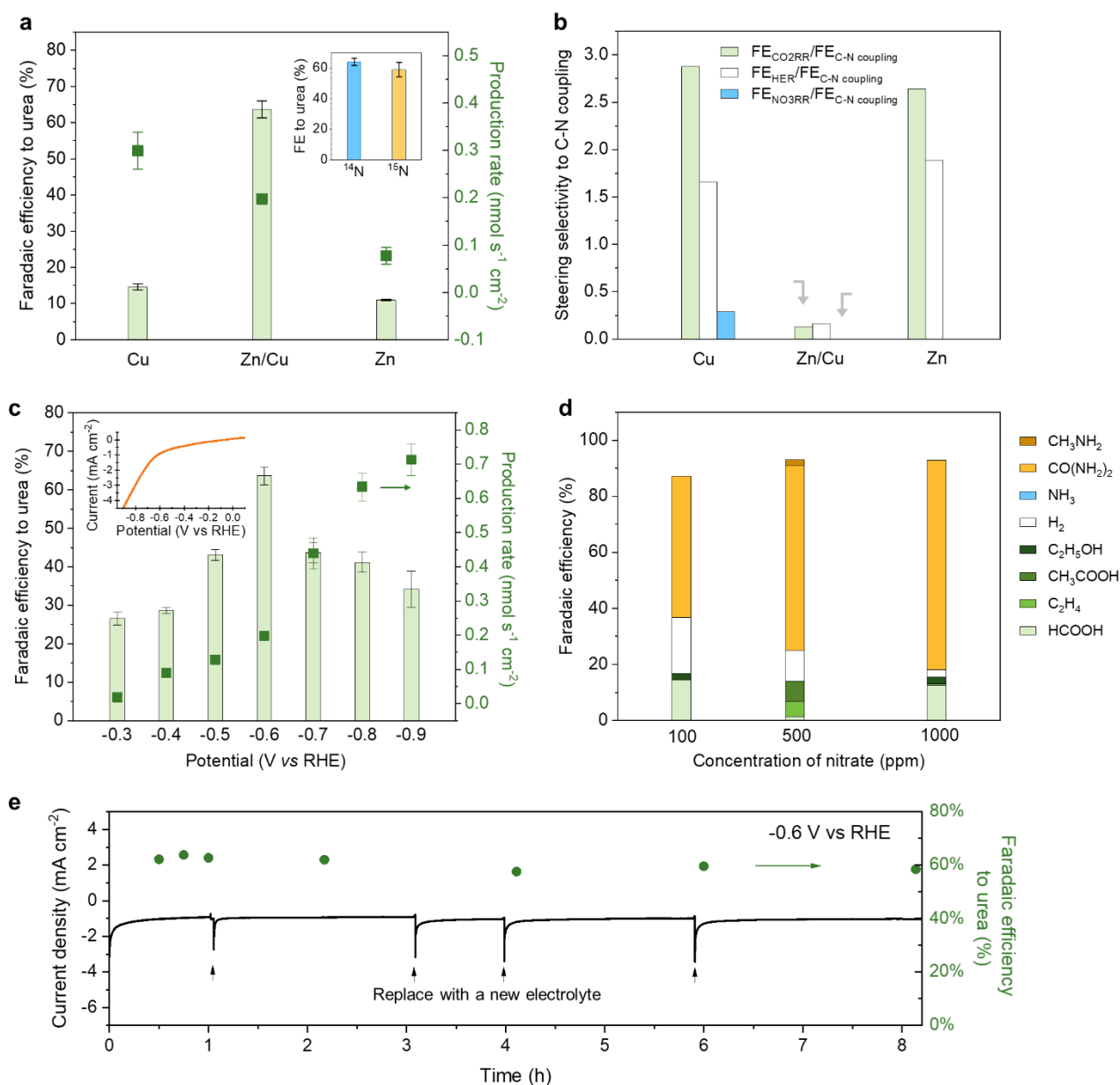

Fig. 3| Steering selectivity to C-N coupling on Zn/Cu hybrid catalysts. a) Faradaic efficiency to urea on the Zn/Cu hybrid catalyst and the single-component counterparts. Insert in (a) is detection of urea by ^{14}N and ^{15}N NMR. **b)** Selectivity to C–N coupling and side reactions. **c, d)** Faradaic efficiency to urea and its production rate on a Zn-0.5/Cu hybrid catalyst under different potentials (c) at different nitrate concentrations (d). Inset in (c) is the linear sweep voltammetry curve for Zn-0.5/Cu. **e)** Stability test on Zn-0.5/Cu hybrid catalyst.

We used in-situ infrared reflection-absorption spectroscopy (IRRAS) to detect intermediates and products across the potential range +0.3 to –1.2 V vs. RHE (Fig. 4a). The infrared bands probed at 1629 and 1175 cm^{-1} originate from the bending and rocking modes of –NH$_2$ in urea, repsectively[22]. The band found at 1314 cm^{-1} is attributed to the wagging mode of –NH$_2$[5]. The infrared band at 1417 cm^{-1}, referring to the stretching mode of C–N bond in urea[23], appears when applying negative potentials but diminishes when elevating the potential to –1.2 V vs. RHE. Compared to the free urea, the stretching frequency of the C–N bond shifts to a lower wavenumber, indicating that the urea is coordinated with metal ions on the hybrid catalyst through an oxygen atom associated with the C=O group[23]. In-situ X-ray absorption spectroscopy shows local electronic structure and local geometric structure of the hybrid catalyst have negligible changes (Supplementary Fig. 18).

From in-situ IRRAS, a band at 1699 cm^{-1} appears starting at –0.3 V vs. RHE and diminishes to near-zero at –1.2 V vs. RHE, the range over which urea synthesis occurs. This band has previously been assigned to C=O in COOHNH$_2$ dimer[24], a carbamate that is usually observed at low temperatures[24]. Compared to the free molecule[24], the stretching frequency of C=O bond shifts to a higher wavenumber, suggesting that the molecule may be coordinated with metal ions on the hybrid catalyst through the hydroxyl oxygen atom of O–C=O. These results attest to the presence of the intermediate *COOHNH$_2$. We also found that an infrared band arose at 1403 cm^{-1} under potentials between 0 and –1.2 V vs. RHE, something we propose is assigned to the OCO vibrational band, consistent with the presence of *CO$_2$NH$_2$[5]. These results agree with the picture in which protonation of CO$_2$NH$_2$ to COOHNH$_2$ is a key step for urea synthesis.

For comparison, we performed the IRRAS on single-component Zn and Cu. On the Zn, a weak band arises at 1398 cm^{-1} (*CO$_2$NH$_2$) when the potential is between –0.3 and –1.2 V vs. RHE, but no band near 1699 cm^{-1} (*COOHNH$_2$) (Supplementary Fig. 19). The rate-determining step on Zn is therefore suggested as the protonation of *CO$_2$NH$_2$ to form *COOHNH$_2$. On the Cu, we did not observe bands near 1398 cm^{-1} nor 1699 cm^{-1} (Supplementary Fig. 19). This can be explained if the first C–N bond formation is a rate-determining step on Cu.

We also used in-situ surface-enhanced Raman spectroscopy (SERS) to detect intermediates on the Zn/Cu hybrid catalyst (Figure 4b). Ammonium carbamate (NH$_2$COONH$_4$, AC) was used as a reference that consists of CO$_2$NH$_2^-$ in aqueous solutions, together with ions NH$_4^+$, HCO$_3^-$ and

CO_3^{2-}. The same peak at 334–337 cm^{-1}, the feature assigned to M–OCONH$_2$ (*CO$_2$NH$_2$), was detected under urea synthesis conditions (left panel) and in the AC solution (middle panel), but not in KHCO$_3$ solution (right panel) nor in other control conditions (Supplementary Figs. 20). The *CO$_2$NH$_2$ signal was observed at about –0.5 V vs. RHE under urea synthesis conditions and –0.3 V in the AC solution. On single-component Cu, we observed only the *CO$_2$NH$_2$ signal in the AC solution starting at –0.1 V vs. RHE (Supplementary Figs. 21-22). These results are in line with the view that Zn contributes to the formation of the needed *CO$_2$NH$_2$ intermediate.

DFT calculations were used to study further the functions of Zn and Cu in hybrid catalysts (Figs. 4c-4d). Following adsorption and reduction of NO$_3^-$ on the Zn surface (step 1), a CO$_2$ molecule inserts to form C–N bond, with its oxygen atom bonded to another Zn atom to form *CO$_2$NO$_2$ (step 2). This step is more energetically favorable on the Zn surface rather than on the Cu (Fig. 4b). The reaction energy for step 9 is higher on the Zn surface (~1.8 eV) than on the Cu surface (~0.5 eV) corresponding to the protonation of *CO$_2$NH$_2$ to form *COOHNH$_2$ (Fig. 4c), which suggests that Cu surface is necessary to accomplish a catalytic loop for urea synthesis following a relay catalysis pathway. In this way, the reaction energy for the two steps: (i) C–N bond formation step (intermediate *CO$_2$NO$_2$) and (ii) protonation step (intermediate *COOHNH$_2$), are independently tuned by the Zn/Cu hybrid catalyst.
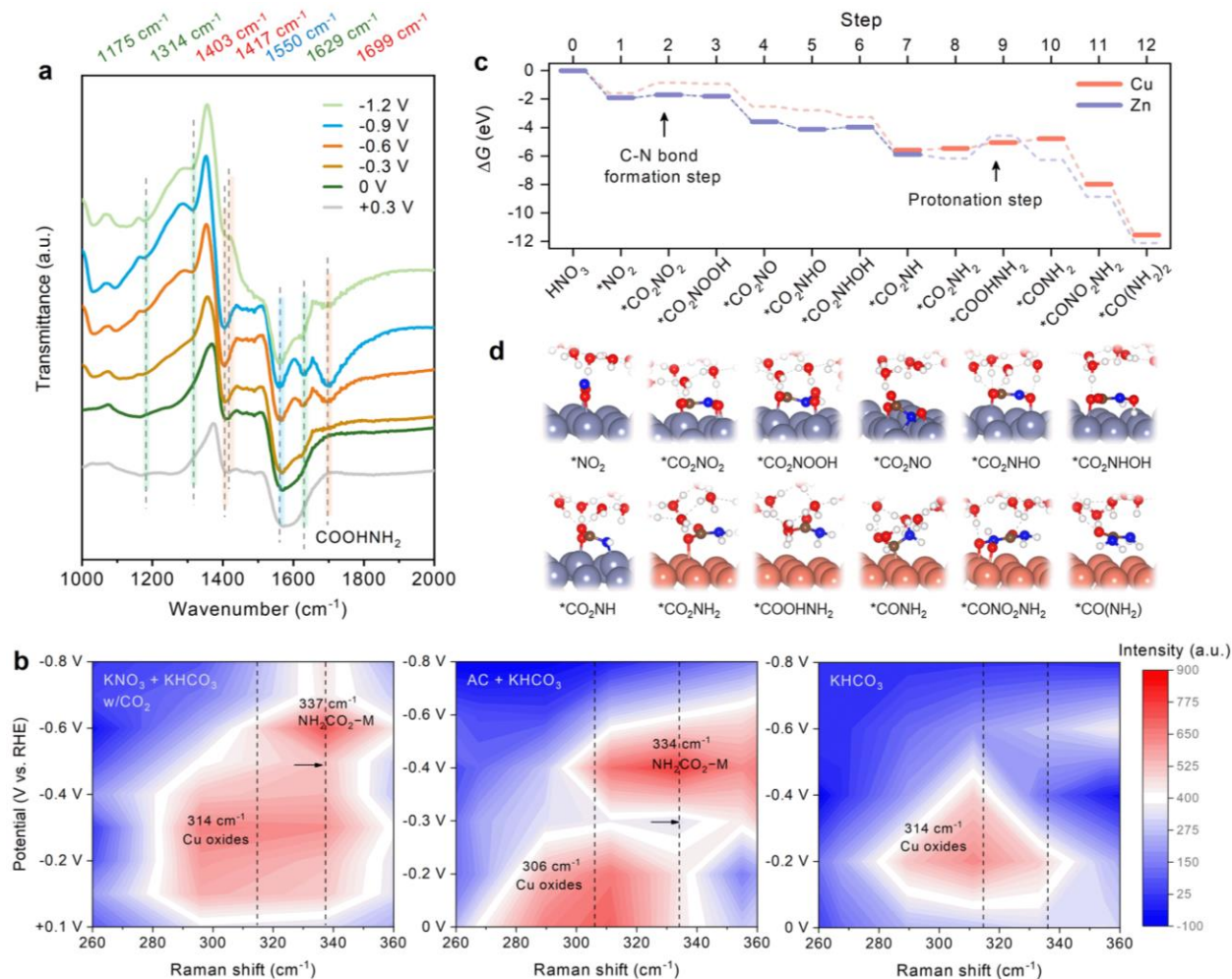
Fig. 4| Mechanistic study elucidating a chemical picture of relay catalysis. a) In-situ IRRAS and **b)** in-situ SERS measurements on Zn/Cu under various potentials. **c)** DFT calculations of the free energy diagram for the synthesis of urea from NO_3^- and CO_2 and **d)** corresponding atomic configurations for each step. Orange, grey, red, blue, brown and white denote Cu, Zn, O, N, C and H, respectively. Zn surface is, after a $*NO_2$ being adsorbed (step 1), more energetically favourable to the C–N bond formation to form $*CO_2NO_2$ (step 2, insertion of a CO_2 molecule) than the Cu surface, while the latter diminishes the reaction energy for the potential-determining protonation step on Zn (step 9) so as to complete a catalytic loop.

To assess the prospects from a one-step electrosynthesis of urea, we calculated the global warming potential and energy cost, compared to the Haber-Bosch process. In an energy analysis of the inert nitrogen-mediated cycle, looking at urea production and biological denitrification of

wastewater (Supplementary file 2), cycling each ton of urea (0.47 ton N) costs ~30 GJ for synthesis and between 50 and 160 GJ for denitrification (Supplementary file 2). This process (Fig. 5a) emits greenhouse gases with a total global warming potential of 24 – 32 ton CO_2 equivalent (CO_2e). The major contributors are CO_2 from the combustion of fossil fuels to power the Haber-Bosch and Bosch-Meiser processes, and GHGs such as CH_4 and N_2O emitted in biological denitrification.

The one-step active nitrogen-mediated cycle is projected to emit GHGs with a net GWP of ~8 ton CO_2e (Fig. 5a). The net emission of the CO_2 componnt is (cradle-to-gate) negative because the process consumes CO_2 and avoids fossil emissions. Cycling each ton of urea by this process costs ~130 GJ, mainly from electricity (Supplementary file 2). A sensitivity analysis (Fig. 5b) emphasizes the importance of further work on increasing urea FE in reducing energy cost. With 500 or 1000 ppm NO_3^- [N] feeds, the impact of changing 20% FE is twice of changing by 20% the cell voltage.
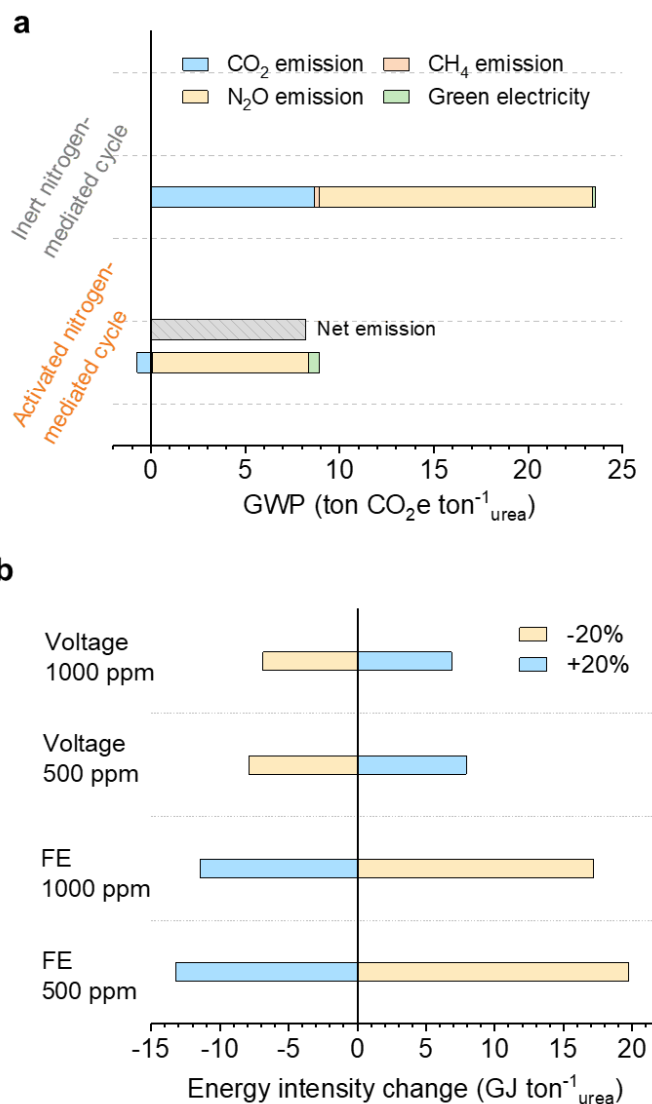
Fig. 5| GWP and energy analysis. a) Global warming potential (GWP) estimated for the inert- and activated-nitrogen mediated cycles. **b)** Sensitivity of the energy intensity to the voltage and faradaic efficiency (FE) for the one-step synthesis of urea electrosynthesis.

The hybrid catalyst studied herein provides an advance in urea selectivity, achieving 75% faradaic efficiency in simulated wastewater containing 1000 ppm NO_3^- [N]. Control experiments, in-situ spectroscopy and calculations paint a picture wherein the Zn/Cu hybrid catalyst enables independent tailoring of barrier energies for each of the two steps (the first C–N bond formation step and the protonation step from $*CO_2NH_2$ to $*COOHNH_2$), thus providing a relay catalysis path, enabling the increase in urea selectivity.

Methods

Chemicals. Potassium nitrate (KNO_3), potassium hydrogen carbonate ($KHCO_3$), ammonium carbamate (NH_4COONH_2, AC), Zn nanoparticles (average sizes of 40 – 60 nm, ≥99% trace), and Cu nanoparticles (average sizes of 25 nm, TEM) were purchased from Signa-Aldrich. Bipolar membranes were received from Fuel Cell Store. The copper target (99.999%) for e-beam deposition was purchased from Kurt J. Lesker. Polytetrafluoroethylene membrane with an average pore size of 450 nm was received from Beijing Zhongxingweiye Instrument. All chemicals used in this work were used as received. The aqueous solutions were prepared using distilled water with a resistivity of 18.2 MΩ cm with a UV radiation accessory.

Catalyst preparation. Single-component Cu catalysts were prepared by sputtering Cu (200 nm) on polytetrafluoroethylene (PTFE) fiber substrate or spray coating Cu nanoparticle ink onto carbon paper (Freudenberg H23C9, Fuel Cell Store) with a hydrophobic treatment layer. Single-component Zn catalysts were prepared by spray coating Zn nanoparticle ink onto carbon paper. 16 ul Nafion (5%) was also added into 16 ml methanol and 8 mg nanoparticles (Cu or Zn), and then was sonicated for 1 h to prepare Cu or Zn nanoparticle inks. The Cu or Zn nanoparticle inks were spray-coated onto the carbon paper with a loading of ~2 mg cm^{-2} and dried under atmosphere, then stored in glove box before electrochemical tests. The Zn/Cu hybrid catalysts are prepared by spray-coating Zn nanoparticle ink onto a sputtered Cu or a spray-coated Cu film depending on what electrode configuration of hybrid catalyst is prepared. For the sputtered Cu film, e-beam evaporation is applied using a Cu target at a deposition rate of ~ 1 Å s^{-1} to get a film thickness of ~200 nm on a porous PTFE fiber substrate[25]. The loading amounts of Zn nanoparticles are controlled during spray coating. Other mono-component and hybrid catalysts were prepared by spray coating corresponding nanoparticle inks on substrates, and the preparation method of these inks is same to that of Cu ad Zn inks.

Electrochemical performance. The electrochemical data were collected using an electrochemical station (PGSTAT204) in a flow cell system, with catalysts to be measured as the cathode, Ag/AgCl electrode the reference electrode, and nickel foam the counter electrode. The catholytes varied for different test purpose, and its is 0.1 M $KHCO_3$ with 500 ppm KNO_3 [N] unless otherwise specified. The anolyte was always 1 M KOH solution. A bipolar membrane was used to separate the anolyte and catholyte. Before reaction, the catholyte was purged with CO_2 or Ar depending on the purpose

of tests. During reaction, CO_2 gas is feeding from a GDL at flow rate of 30 s.c.c.m. To detect the gaseous products probably of tiny amounts such as H_2, CO, and NH_3, a slow flow rate of 1 s.c.c.m was used that was controlled by an electromagnetic flowmeter. The catholyte and anolyte were circulated using a peristaltic pump.

The potentials (E) in were converted to values versus the reversible hydrogen electrode (RHE).

$$E_{RHE} = E_{Ag/AgCl} + 0.198 + 0.0591 \times pH$$

$$E_{RHE} = E_{SCE} + 0.24 + 0.0591 \times pH$$

Characterization. The morphology and elemental distributions of sample was examined by field emission SEM (5 kV, Hitachi, SU5000). The XRD (MiniFlex600) pattern was collected with Cu Kα as the radiation source. The high-resolution TEM analyses were collected at an electron acceleration voltage of 300 kV (FET Tecnai F30). The high-resolution XPS (Thermo Fisher ECSALAB 250Xi) spectrum were collected using monochromatic Al Kα X-rays, and the pass energy was 20 eV and energy step size was 0.1 eV. Depth profile was achieved by Ar bombardment in the chamber.

In the in-situ IRRAS characterization, the carbon paper was used as substrate/GDL. The hybrid catalyst was used as the cathode in electrolytes of 0.1 M $KHCO_3$ with 0.1 M KNO_3 saturated by CO_2. Pt wire is used as the anode electrode, and Ag/AgCl the reference electrode. The in-situ IRRAS spectra were collected using a Nicolet IS50 spectrometer equipped with a mercuric cadmium telluride (MCT) detector. For the control IRRAS experiment, Ar was purged into a solution (0.1 M $KHCO_3$ and 0.1 M KNO_3) until saturated.

In the XAS characterization, the carbon paper was used as substrate/GDL. The hybrid catalyst was used as the cathode in electrolytes of 0.1 M $KHCO_3$ with 0.1 M KNO_3 saturated by CO_2. Pt wire is used as the anode electrode, and SCE the reference electrode. The XAS spectra at the Cu and Zn K-edges were recorded at the BL11B beamline of Shanghai Synchrontron Radiation Facility (SSRF). The beam current of the storage ring was 220 mA in a top-up mode. The incident photons were monochromatized by a Si (111) double-crystal monochromator, with an energy resolution $\Delta E/E$ ~1.4×10^{-4}. The spot size at the sample was ~ 200 μm. All the operando XAFS spectra at the Cu and Zn K-edge were collected in a fluorescence mode.

In the in-situ SERS characterization, different conditions were used, including urea synthesis condition (1 M $KHCO_3$ + 1 M KNO_3), AC reference condition (0.03 M AC + 0.7 M $KHCO_3$), $KHCO_3$ (1 M $KHCO_3$), K_2CO_3 (1 M K_2CO_3), and KNO_3 (1 M KNO_3). The characterization was performed on a Renishaw inVia Raman spectrometer in a modified flow cell and a water immersion objective (×63) with a 785 nm laser with a 0.5% power, using a 10 s integration and accumulation 4 scans per region. Pt wire and Ag/AgCl were used as anode and reference electrodes, respectively.

The gas-phase products, including CO, CH_4, C_2H_4, and H_2, were tested by gas chromatograph (GC, PerkinElmer Clarus 600) equipped with a thermal conductivity detector and a flame ionization detector. The liquid products, including $HCOO^-$, NH_4^+, C_2H_5OH, CH_3COOH, and n-propanol, and CH_3NH_2 were analyzed using ^1H NMR spectrometer (Agilent DD2 600 MHz), using a known amount of acetonitrile as an internal standard. For the detection of NH_3 is also achieved by ^1H NMR, where the electrolyte was acidized to reach pH value of ~3 by addition of an appropriate amount of 0.5 M H_2SO_4. In this study, the UV-vis adsorption spectroscopy was not able to detect NH_3 due to the interference of CO_2RR products. Ionic detector was used to detect N_2, N_2O, NO_x, etc by feeding Ar carrier gas with the flow rate of 1 s.s.c.m.

The product urea was quantified by multiple methods. First, the diacetylmonoxime method is carried out using UV-vis adsorption spectroscopy[26, 27]. The aluminum foil was used to cover the glass bottle containing electrolyte samples before tests to avoid light illumination. The extracted electrolyte was initially subjected to the quantification of urea without any post-processing. Second, the urea was quantified by ^{14}N NMR. The isotope-labelled ^{15}N NMR show different peak positions as compared to the unlabelled ones. For the self-suspicious experiments, all the electrolytes were prepared using distilled water with a resistivity of 18.2 MΩ cm with a UV radiation accessory in a sealed transparent container that was carefully cleaned. Then, the container with electrolytes were irradiated under a UV light for 2 h before electrochemical tests. The tests were carried out instantly after UV irradiation. Clean electrochemical cell and accessories were also used.

Density functional theory (DFT) calculations. All ab initio DFT calculations were performed by employing the projector-augmented wave method as implemented in the Vienna Ab initio Simulation Package[28, 29]. The generalized gradient approximation in the parametrization of Perdew–Burke–Ernzerhof[30] was implemented to describe the exchange-correlation function. A

plane-wave cut-off of 450 eV and $3 \times 3 \times 1$ gamma-centred k-point grids generated by the Monkhorst–Pack[31] scheme were used for all the calculations. A charged water overlayer[32] together with the zero damping DFT-D3 method of Grimme[33] were considered to account for the field and solvation effects as well as long-range van der Waals interactions. A hexagonal charged water overlayer was added on a $3 \times 3 \times 4$ fcc(111) surface of metals (Ag and Cu) and $3 \times 3 \times 4$ hcp(0001) surface on metal (Zn) which includes five water molecules and a hydronium (H_3O^+). A vacuum region of more than 15 Å thickness was included along the perpendicular direction to avoid artificial interactions. All atoms in the bottommost two layers were fixed during the structural optimization, while other atoms together with the adsorbates were allowed to relax. Geometries were optimized by considering different adsorption sites on the surfaces with respect to the charged water overlayer, and the ones with the lowest energy from DFT calculations were reported. Ab initio molecular dynamics simulations were conducted in a constant volume, constant temperature ensemble and performed for 10 ps with the time step set to 0.5 fs, to optimize the structure of charged water overlayer. The Nosé-Hoover thermostat method was used to maintain the temperature at 300 K.

Author contributions

Y.L and K.X proposed the idea and contributed to all experimental works, data analysis and manuscript. P.O. contributed to DFT calculations with the feedbacks from X.L. T.P contributed to in-situ IRRAS experiments. Z.Z and B.L contributed to in-situ XAS characterization. C.C. and Y.L performed the in-situ SERS characterization and analysis. I.G contributed to the discussion of materials. K.X contributed to LCA analysis. D.S contributed to the discussion of this work. E.H.S supervised this study.

Competing interests

The authors declare no competing interests.

References

1. Fowler D*, et al.* The global nitrogen cycle in the twenty-first century. *Philos. T. Roy. Soc. B* **368**, 20130164 (2013).

2. Hattori M, Iijima S, Nakao T, Hosono H, Hara M. Solid solution for catalytic ammonia synthesis from nitrogen and hydrogen gases at 50 degrees C. *Nat Commun* **11**, 2001 (2020).

3. Molecule of the Week Archive Ammonia, *www.acs.org/content/acs/en/molecule-of-the-week/archive/a/ammonia.html*.

4. Molecule of the Week Archive Urea, *www.acs.org/content/acs/en/molecule-of-the-week/archive/u/urea.html*.

5. Lv C*, et al.* Selective electrocatalytic synthesis of urea with nitrate and carbon dioxide. *Nat. Sustain.* **4**, 868–876 (2021).

6. Cogert KI, Ziels RM, Winkler MKH. Reducing cost and environmental impact of wastewater treatment with denitrifying methanotrophs, anammox, and mainstream anaerobic treatment. *Environ. Sci. Technol.* **53**, 12935–12944 (2019).

7. Damma D, Ettireddy P, Reddy B, Smirniotis P. A review of low temperature NH_3–SCR for removal of NO_x. *Catalysts* **9**, 349 (2019).

8. Wu Y, Jiang Z, Lin Z, Liang Y, Wang H. Direct electrosynthesis of methylamine from carbon dioxide and nitrate. *Nat. Sustain.* **4**, 725–730 (2021).

9. Saravanakumar D, Song J, Lee S, Hur NH, Shin W. Electrocatalytic conversion of carbon dioxide and nitrate ions to urea by a titania-nafion composite electrode. *Chemsuschem* **10**, 3999–4003 (2017).

10. Lv C*, et al.* A defect engineered electrocatalyst that promotes high-efficiency urea synthesis under ambient conditions. *ACS Nano* **16**, 8213–8222 (2022).

11. Li J, Zhang Y, Kuruvinashetti K, Kornienko N. Construction of C–N bonds from small-molecule precursors through heterogeneous electrocatalysis. *Nat. Rev. Chem.* **6**, 303–319 (2022).

12. Jouny M*, et al.* Formation of carbon-nitrogen bonds in carbon monoxide electrolysis. *Nat. Chem.* **11**, 846–851 (2019).

13. Tao Z, Rooney CL, Liang Y, Wang H. Accessing organonitrogen compounds via C–N coupling in electrocatalytic CO_2 reduction. *J. Am. Chem. Soc.* **143**, 19630–19642 (2021).

14. Meng N, *et al.* Oxide-derived core-shell Cu@Zn nanowires for urea electrosynthesis from carbon dioxide and nitrate in water. *ACS Nano* **16**, 9095–9104 (2022).

15. Fernandez-Nava Y, Maranon E, Soons J, Castrillon L. Denitrification of wastewater containing high nitrate and calcium concentrations. *Bioresour. Technol.* **99**, 7976–7981 (2008).

16. Moloantoa KM, Khetsha ZP, van Heerden E, Castillo JC, Cason ED. Nitrate water contamination from industrial activities and complete denitrification as a remediation option. *Water* **14**, 799 (2022).

17. Shi L, Liu L, Yang B, Sheng G, Xu T. Evaluation of industrial urea energy consumption (EC) based on life cycle assessment (LCA). *Sustainability* **12**, 3793 (2020).

18. Bargiacchi E, Antonelli M, Desideri U. A comparative assessment of power-to-fuel production pathways. *Energy* **183**, 1253–1265 (2019).

19. Shibata M, Yoshida K, Furuya N. Electrochemical synthesis of urea on reduction of carbon dioxide with nitrate and nitrite ions using Cu-loaded gas-diffusion electrode. *J. Electroanal. Chem.* **387**, 143–145 (1995).

20. Shibata M, Yoshida K, Furuya N. Electrochemical synthesis of urea at gas-diffusion electrodes - IV. Simultaneous reduction of carbon dioxide and nitrate ions with various metal catalysts. *J. Electrochem. Soc.* **145**, 2348–2353 (1998).

21. Wang Y, *et al.* Enhanced nitrate-to-ammonia activity on copper-nickel alloys via tuning of intermediate adsorption. *J. Am. Chem. Soc.* **142**, 5702–5708 (2020).

22. Keuleers R, Desseyn HO, Rousseau B, Alsenoy CV. Vibrational analysis of urea. *J. Phys. Chem. A* **103**, 4621–4630 (1999).

23. Manivannan M. Investigation of inhibitive action of urea–Zn^{2+} system in the corrosion control of carbon steel in sea water. *Int. J. Eng. Sci. Tech.* **3**, 8084–8060 (2011).

24. Bossa JB, Theulé P, Duvernay F, Borget F, Chiavassa T. Carbamic acid and carbamate formation in $NH_3:CO_2$ ices – UV irradiation versus thermal processes. *Astron. Astrophys.* **492**, 719–724 (2008).

25. Arquer FPGd, *et al.* CO_2 electrolysis to multicarbon products at activities greater than 1 A cm^{-2}. *Science* **367**, 661–666 (2020).

26. Rahmatullah M, Boyde TRC. Improvements in the determination of urea using diacetylmonoxime; Methods with and without deproteinization. *Clin. Chim. Acta.* **107**, 3–9 (1980).

27. Chen C, *et al.* Coupling N_2 and CO_2 in H_2O to synthesize urea under ambient conditions. *Nat. Chem.* **12**, 717–724 (2020).

28. Kresse G, Hafner J. Ab initio molecular dynamics for liquid metals. *Physical Review B* **47**, 558–561 (1993).

29. Kresse G, Hafner J. Ab initio molecular-dynamics simulation of the liquid-metal--amorphous-semiconductor transition in germanium. *Physical Review B* **49**, 14251–14269 (1994).

30. Perdew JP, Burke K, Ernzerhof M. Generalized gradient approximation made simple. *Physical Review Letters* **77**, 3865–3868 (1996).

31. Monkhorst HJ, Pack JD. Special points for Brillouin-zone integrations. *Physical Review B* **13**, 5188–5192 (1976).

32. Montoya JH, Shi C, Chan K, Nørskov JK. Theoretical insights into a CO dimerization mechanism in CO_2 electroreduction. *The Journal of Physical Chemistry Letters* **6**, 2032–2037 (2015).

33. Grimme S, Antony J, Ehrlich S, Krieg H. A consistent and accurate ab initio parametrization of density functional dispersion correction (DFT-D) for the 94 elements H-Pu. *The Journal of Chemical Physics* **132**, 154104 (2010).